


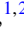


Topological phases of ultracold molecules in an optical tweezer ladderJinzu Jiang ^{1,2}, Jia-Hui Zhang ^{1,2}, Feng Mei ^{1,2,*}, Zhonghua Ji ^{1,2,†}, Ying Hu,^{1,2} Jie Ma,^{1,2} Liantuan Xiao,^{1,2,‡} and Suotang Jia^{1,2}¹*State Key Laboratory of Quantum Optics and Quantum Optics Devices, Institute of Laser Spectroscopy, Shanxi University, Taiyuan, Shanxi 030006, China*²*Collaborative Innovation Center of Extreme Optics, Shanxi University, Taiyuan, Shanxi 030006, China*

(Received 19 February 2022; accepted 16 August 2022; published 25 August 2022)

The recent experimental realization of optical tweezer arrays of ultracold molecules provides a versatile platform for exploring molecular phases of matter. Here we show that by programming tweezers, the dipolar interactions in an optical tweezer ladder could be tailored to implement a generalized Su-Schrieffer-Heeger model. Through calculating topological invariants, nonlocal string-order parameters, many-particle ground-state degeneracy, and entanglement spectrum, we demonstrate that this ladder at the single-particle level supports two different chiral topological phases and at the many-particle level features two different interacting topological phases and, respectively, possesses much richer topological edge states. We also discuss the detection of these topological phases and their robustness to systematic imperfections. Further generalization to a high dimension could offer opportunities for preparing diverse ultracold molecular topological phases.

DOI: [10.1103/PhysRevA.106.023318](https://doi.org/10.1103/PhysRevA.106.023318)**I. INTRODUCTION**

Ultracold molecules possess rich internal structures and long-range dipolar interactions, as compared to ultracold neutral atoms. Leveraging these unique properties, ultracold molecule systems promise unique directions in quantum computation [1–7] and simulation [8–18], quantum chemistry [19,20], and precision measurements [21,22]. To realize the full potential of such a system, large-scale ultracold molecular arrays combined with full quantum control on individual molecules are required. The past three years have witnessed rapid experimental progress in scaling up ultracold molecular arrays via optical tweezers [23–36], including the creation of optical tweezer arrays of rovibrational ground-state molecules [36] and the improvement of rotation coherence time to nearly 100 milliseconds in optical tweezers [32]. With the success of this bottom-up approach, ultracold molecular tweezer arrays are becoming a scalable quantum platform for quantum science applications [23,37–39], particularly for quantum simulation of exotic phases of matter.

Topological phases of matter are now of great interest across many areas of physics [40–48]. Distinct from conventional phases, topological phases are protected by global topological invariants and therefore inherit natural robustness against perturbations and noises, enabling both fascinating physics and exciting applications. By engineering sophisticated external fields to manipulate the dipolar interactions,

previous studies have shown that topological phases could be implemented in ultracold dipolar molecules based on optical lattices, including topological flat bands [49,50], fractional Chern insulators [51], Weyl excitations [52], and Hopf topological insulator phases [53,54]. However, this system lacks the ability to create arbitrary geometry of topological lattices and *in situ* manipulate the position-dependent dipolar interaction, thereby limiting its flexibility and versatility. An alternative route is to use programmable optical tweezer arrays, which allows us to create arbitrary lattice geometry and arbitrary boundaries and tune the position-dependent dipolar interactions into wanted spatial anisotropy [23]. A recent experiment has demonstrated that the paradigmatic topological Su-Schrieffer-Heeger model can be naturally implemented by using optical tweezer arrays of Rydberg atoms [55].

In this paper, we investigate topological phases of ultracold molecules in optical tweezer arrays. Through programming optical tweezer configurations, we show that the dipolar interactions in an optical tweezer ladder could be tailored to implement a generalized Su-Schrieffer-Heeger model. Compared to the standard one, as we will show, this model supports two different nontrivial topological phases and has two different kinds of topological edge states, both in the single- and many-particle case. As for the previous case, this ladder system possesses two nontrivial chiral topological phases, distinguished by two different topological winding numbers, signified by the single-particle edge states with quite different localization features. We also present a method to directly probe both the topological winding numbers and topological edge states by using spin dynamics. Furthermore, we study the topological phases in the many-particle case, basing on exact diagonalization and density matrix renormalization group calculations. The numerical results of nonzero string-

*meifeng@sxu.edu.cn

†jzh@sxu.edu.cn

‡xlt@sxu.edu.cn

order parameters indicate that the optical tweezer ladder system supports two different interacting symmetry-protected topological (SPT) phases, featuring fourfold degeneracy of ground states, twofold degeneracy of entanglement spectra, and two different edge states in the quasiparticle energy spectra. We also exhibit that in both cases these topological phases are robust to systematic imperfections.

The paper is organized as follows. Section II presents how to realize a generalized Su-Schrieffer-Heeger model from molecular dipolar interactions in an optical tweezer ladder. Section III studies the single-particle topological properties and their detection. Section IV investigates the topological properties of interacting SPT phases and their robustness. Section V gives a summary and outlook for this paper.

II. ULTRACOLD MOLECULES IN AN OPTICAL TWEezer LADDER

We consider ultracold polar molecules trapped in an optical tweezer array with one molecule per tweezer. Motivated by recent experiments [25,36], we could choose NaCs or CaF as our molecular species. As demonstrated below, by encoding two rotational states into a spin, the dipolar interaction between polar molecules realizes a spin-exchange interaction and the exchanging of a spin-up state between tweezers simulates the hopping of a hard-core boson between lattice sites. Specifically, the dipole-dipole interaction between molecules is given by

$$H_{dd} = \frac{1}{2} \sum_{i \neq j} \frac{\kappa}{R_{ij}^3} [\mathbf{d}_i \cdot \mathbf{d}_j - 3(\mathbf{d}_i \cdot \mathbf{R}_{ij})(\mathbf{d}_j \cdot \mathbf{R}_{ij})], \quad (1)$$

where $\kappa = 1/4\pi\epsilon_0$, \mathbf{d}_i is the dipole moment of molecule i and \mathbf{R}_{ij} is the vector connecting the two molecules i and j . In the spherical coordinates, the dipole-dipole interaction can be rewritten in spherical tensor form as

$$H_{dd} = -\frac{\sqrt{6}}{2} \sum_{i \neq j} \frac{\kappa}{R_{ij}^3} \sum_{p=-2}^2 (-1)^p C_{-p}^2(\theta, \phi) T_p^2(\mathbf{d}_i, \mathbf{d}_j), \quad (2)$$

where $C_{-p}^2(\theta, \phi) = \sqrt{\frac{4\pi}{5}} Y_{2,-p}(\theta, \phi)$ and the spherical tensors are given by $T_{\pm 1}^2 = (d_i^z d_j^\pm + d_i^\pm d_j^z)/\sqrt{2}$, $T_{\pm 2}^2 = d_i^\pm d_j^\pm$, $T_0^2 = (d_i^- d_j^+ + 2d_i^z d_j^z + d_i^+ d_j^-)/\sqrt{6}$. As illustrated in Fig. 1(a), the optical tweezer array is confined to the x - z plane and arranged into a structure of two-leg ladder geometry. With respect to this configuration, θ is the angle between the z axis and the vector \mathbf{R}_{ij} and $\phi = 0$.

Each ultracold polar molecule trapped in an optical tweezer could mimic a spin. As for this paper, we investigate the spin-1/2 case where the two spin states are encoded by two rotational states, i.e., $|\uparrow\rangle = |0, 0\rangle$ and $|\downarrow\rangle = |1, -1\rangle$ [15]. In the absence of electric fields, by projecting the Hamiltonian H_{dd} into the Hilbert space spanned by $\{|\uparrow\rangle, |\downarrow\rangle\}$, we obtain a spin-exchange interaction Hamiltonian,

$$H = \sum_{i>j} J_{ij} (S_i^+ S_j^- + S_i^- S_j^+), \quad (3)$$

where S_i^\pm is the spin raising operator on the site i and $J_{ij} = -\kappa d_{\uparrow\downarrow}^2 V_{dd}(\mathbf{R}_{ij})/2$ is the long-range spin-exchange interaction

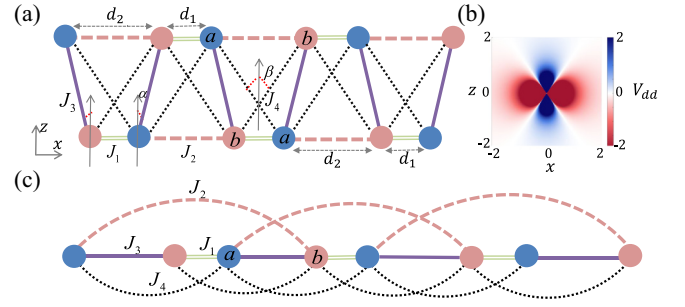


FIG. 1. (a) An optical tweezer ladder in which each tweezer traps a single molecule. The quantization axis set by the magnetic field is oriented along the z direction. By reconfiguring optical tweezers, two coupled dimerized optical tweezer chains are naturally implemented, which can be described by a dimerized hard-core lattice model as shown in (c), with two sublattices a and b . (b) The geometric factor $V_{dd}(\mathbf{R}_{ij})$ between the origin and the tweezer site (x, z) .

strength. $d_{\uparrow\downarrow} = \langle \uparrow | d^+ | \downarrow \rangle$ is the transition dipole moment. The long-range feature is manifested by the geometric factor $V_{dd}(\mathbf{R}_{ij}) = (1 - 3\cos^2(\theta))/R_{ij}^3$ shown in Fig. 1(b). An interesting feature is that the long-range spin-exchange interaction could vanish when the angle is tuned to $\theta_c = \pm \arccos(1/\sqrt{3})$, irrespective of \mathbf{R}_{ij} .

The superiority for using optical tweezers is that the spatial anisotropy of spin-exchange interaction could be tuned by controlling the tweezer locations to engineer \mathbf{R}_{ij} and θ . As displayed in Fig. 1(a), the tweezers in each leg are arranged along the x direction, which gives $\theta = \pi/2$, so the spin-exchange interaction strengths for the x direction are only dependent on the distances R_{ij} . With this feature, by controlling the separation distances d_1 and d_2 to separately tune J_1 and J_2 , two dimerized spin chains are naturally implemented in the two legs, where each unit cell has two spins, labeled by a and b . Between the two legs, the spin-exchange couplings are also dependent on θ , which allows us to turn on or off the couplings. For example, by arranging the tweezer configuration to make $\alpha = \theta_c$ or $\beta = \theta_c$, one can, respectively, turn off the intraleg couplings J_3 or J_4 . As calculated in Fig. 1(b), the couplings beyond nearest neighbors are much smaller than the nearest-neighbor couplings $J_{1,2,3,4}$. As we will show, the topological properties of the system can be qualitatively captured by the nearest-neighbor couplings, and the influence of the couplings beyond nearest neighbors is minor.

The spin-exchange interaction model could be mapped to a hard-core lattice model, where the spin-up state is referred to as a hard-core bosonic excitation and the spin-down state as the absence of such an excitation. As depicted in Fig. 1(c), the optical tweezer ladder can be described by a generalized hard-core Su-Schrieffer-Heeger model [56], with the corresponding hard-core lattice Hamiltonian written as

$$H = \sum_{j=1}^N J_1 b_j^\dagger a_{j+1} + J_2 a_j^\dagger b_{j+1} + J_3 a_j^\dagger b_j + J_4 a_j^\dagger a_{j+1} + J_4 b_j^\dagger b_{j+1} + \text{H.c.}, \quad (4)$$

where $a^\dagger (b^\dagger) = S_a^+ (S_b^+)$ is the bosonic creation operator. The single molecules in each tweezer are initially prepared into

the spin-down state that also can be flipped into the spin-up state through microwave pulses. As a result, the number of hard-core boson particles (spin-up states) in this system can be precisely manipulated by controlling the number of excited molecules in the tweezer array, which allows us to study both noninteracting single-particle and interacting many-particle topological phases.

III. NONINTERACTING SINGLE-PARTICLE TOPOLOGICAL PHASES

A. Noninteracting topological phases

We first study single-particle topological phases in the optical tweezer ladder model. For this purpose, we transfer the real space single-particle Hamiltonian H into the momentum space through a Fourier transformation, which gives $H(k_x) = \sum_{k_x} c^\dagger(k_x) h(k_x) c(k_x)$, where $c(k_x) = [a(k_x), b(k_x)]^T$,

$$h(k_x) = h_0(k_x)I + h_x(k_x)\sigma_x + h_y(k_x)\sigma_y, \quad (5)$$

with

$$\begin{aligned} h_0 &= 2J_4 \cos(k_x), & h_x &= J_3 + (J_1 + J_2) \cos(k_x), \\ h_y &= (J_1 - J_2) \sin(k_x). \end{aligned} \quad (6)$$

The Bloch Hamiltonian $h(k_x)$ respects a chiral symmetry when $J_4 = 0$, i.e., $\Gamma h(k_x) \Gamma^{-1} = -h(k_x)$, where $\Gamma = \sigma_z$ is the chiral symmetry operator. As shown in Fig. 1(a), the coupling $J_4 = 0$ is realized by arranging the optical tweezer configuration to adjust $\beta = \theta_c$. The topological properties for the corresponding energy bands are characterized by topological winding numbers, defined as

$$\nu = \frac{1}{2\pi} \int (n_x \partial_{k_x} n_y - n_y \partial_{k_x} n_x) dk_x, \quad (7)$$

where $(n_x, n_y) = (h_x, h_y)/|h|$. Substituting Eqs. (6) into Eq. (7), the topological winding number values are analytically calculated as

$$\nu = \begin{cases} 1, & |J_1 + J_2| > |J_3| \text{ and } |J_1| > |J_2| \\ -1, & |J_1 + J_2| > |J_3| \text{ and } |J_1| < |J_2| \\ 0, & |J_1 + J_2| < |J_3|. \end{cases} \quad (8)$$

This result shows that, in addition to the trivial topological phase $\nu = 0$, our system also supports two different nontrivial topological phases $\nu = \pm 1$.

In experiment, by arranging the optical tweezer configurations in the two legs, one can vary the ratio d_1/d_2 to tune $J_{1,2,3}$, and at the same time fix the angle β to θ_c so $J_4 = 0$. The topological winding number value as a function of d_1/d_2 is numerically calculated in Fig. 2(a). We find that $\nu = 1$ for $d_1/d_2 < 0.54$, $\nu = 0$ for $0.54 < d_1/d_2 < 1.86$, and $\nu = -1$ for $d_1/d_2 > 1.86$. As a consequence, optical tweezer ladders could be expediently tuned into different topological phases and utilized to explore topological phase transitions.

B. Bulk-edge correspondence

Bulk-edge correspondence is a basic theorem associated with topological phases. According to the bulk-edge correspondence, the topological invariant values determine the number of topological edge modes. As an illustration, we

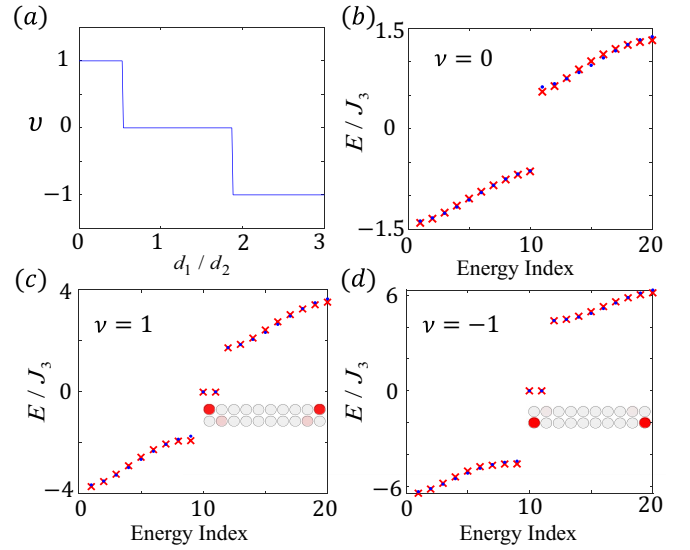


FIG. 2. (a) Topological winding number values as a function of d_1/d_2 . (b)–(d) Edge-state energy spectra of three different topological phases without (dots) and with (crosses) the couplings beyond nearest neighbors. The systematic parameters are (b) $d_2 = 1.2d_1$, $J_1 = -0.25J_3$, and $J_2 = -0.14J_3$, (c) $d_2 = 2.5d_1$, $J_1 = -2.54J_3$, and $J_2 = -0.16J_3$ and (d) $d_2 = d_1/3$, $J_1 = -0.19J_3$, and $J_2 = -5.19J_3$. The density distributions in the tweezer ladder for the two zero-energy modes are shown in the insets of (c), (d). The other parameters are $\beta = \theta_c$ and $J_4 = 0$. J_3 is used as the energy unit.

study such correspondence through the three topological phases $\nu = 0, \pm 1$ shown in Fig. 2(a). By numerically calculating the real-space energy spectra of H in the subspace of single spin-up excitation and in the presence of open boundary conditions (OBCs), the edge-state energy spectra for the three topological phases are shown in Figs. 2(b)–2(d). As shown, for the trivial topological phase $\nu = 0$, there are no zero-energy topological edge modes in the OBC energy spectrum, whereas for the nontrivial topological phase $\nu = \pm 1$, there are one pair of zero-energy topological edge modes, manifested by the particle density distributions shown in the insets of Figs. 2(c) and 2(d). Although the two nontrivial topological phases cannot be distinguished from whether having zero-energy edge modes, the localization features for the edge-state wave functions allows us to distinguish them. Specifically, the left topological edge states in the topological phases $\nu = 1$ ($\nu = -1$) only occupy the a -type (b -type) sublattices and maximally inhabits the leftmost a -type (b -type) tweezer, whereas for the right topological edge states, the situation is opposite. Such different internal structures can be used to promote robust quantum state transfer via topological edge states [57].

C. The influences of long-range couplings

In Figs. 2(b)–2(d), we also study the influence of long-range couplings (beyond nearest neighbors) on the zero-energy topological edge modes. This is done by quantitative comparison of the OBC energy spectra of the system between without (dots) and with (crosses) long-range couplings. It

turns out that the zero-energy topological edge modes are quite robust to the presence of smaller long-range couplings. The reason is that, in the presence of long-range couplings between different sublattices, the system still respects chiral symmetry, which guarantees that the in-gap zero-energy topological edge modes remain intact if $J_{1,2,3}$ dominate those couplings, which is the case for our system, whereas for the long-range couplings between the same sublattices, which break the chiral symmetry and shift the zero-energy modes to non-zero energies, but the in-gap edge modes still exist provided those couplings are not large enough to mix the two energy bands. For our system, the long-range couplings between the same sublattices are very small, so the zero-energy features for the in-gap edge modes nearly remain unchanged. In the insets of Figs. 2(c) and 2(d), we find that the couplings beyond nearest neighbors also do not affect the edge localization features for the two zero-energy modes. Therefore, the couplings beyond nearest neighbors have very little effects, and the essential topological features can be qualitatively determined by the nearest-neighbor couplings $J_{1,2,3}$.

D. Experimental detection

For ultracold molecules, quantum dynamics of spin states governed by the spin-exchange interaction have been experimentally observed in optical lattices by using coherent microwave spectroscopy technique [15]. Here we show that, with such dynamics in an optical tweezer ladder, both the topological invariants and the topological edge states could be directly detected, which thus provides an experimentally accessible method for detecting ultracold molecular topological phases.

To detect the bulk topological invariants, we use a microwave pulse to flip one of the single molecules that is trapped in the bulk of the optical tweezer ladder into a spin-up rotational state. The resulting single spin-up excitation state being the initial state of the system is written as $|\psi(t=0)\rangle = |\downarrow\downarrow\cdots\uparrow\cdots\downarrow\downarrow\rangle$. After an evolution time t , the final state of the system becomes $|\psi(t)\rangle = e^{-iHt}|\psi(0)\rangle$. The winding number can be detected from such spin dynamics by the time-resolved mean chiral displacement

$$C(t) = \langle\psi(t)|X_c|\psi(t)\rangle, \quad (9)$$

where $X_c = \sum_x x(a_x^\dagger a_x - b_x^\dagger b_x)$ is the chiral displacement operator. In the long-time limit, there is a relationship between the winding number value and the time-averaged mean chiral displacement $\bar{C} = \lim_{T \rightarrow \infty} \frac{1}{T} \int_0^T dt C(t)$ [58], i.e.,

$$\nu = 2\bar{C}, \quad (10)$$

where \bar{C} can be seen as the oscillation center of the time-resolved mean chiral displacement $C(t)$, which has been experimentally measured in cold atom systems [59,60]. We notice that the chiral displacement operator is exactly the chiral polarization operator. It was previously found that the chiral polarization corresponding to the Wannier function is equal to half the topological winding number [61]. This implies that the time-averaged mean chiral displacement indeed measures the chiral polarization and explains why it can be connected with the topological winding number.

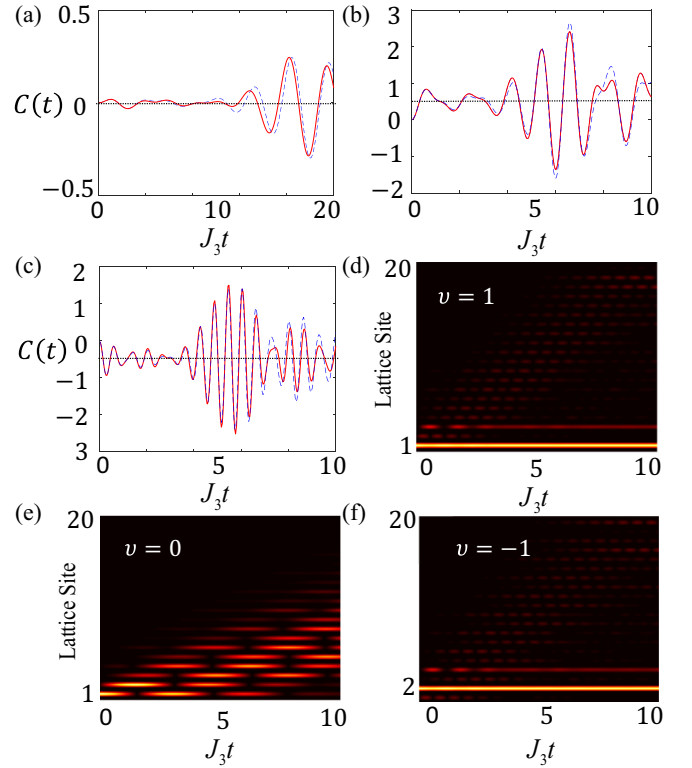


FIG. 3. (a)–(c) Mean chiral displacements versus evolution time, without (solid line) and with (dashed line) long-range couplings. (d)–(f) Time evolution of spin-up density distribution for the cases where the single molecules trapped at the leftmost (d), (e) a -type, and (f) b -type tweezers are initially prepared into the spin-up state. For clear illustration, the tweezer ladder with 20 tweezers is mapped into a linear lattice. The systematic parameters are (a), (e) $d_2 = 1.2d_1$, $J_1 = -0.25J_3$, and $J_2 = -0.14J_3$, (b), (d) $d_2 = 2.5d_1$, $J_1 = -2.54J_3$, and $J_2 = -0.16J_3$ and (c), (f) $d_2 = d_1/3$, $J_1 = -0.19J_3$, and $J_2 = -5.19J_3$.

The time evolution of the mean chiral displacements is numerically calculated in Figs. 3(a)–3(c). When the system is tuned into $|J_1 + J_2| < |J_3|$, as shown in Fig. 3(a), the oscillation center for $C(t)$ is around 0m whereas into $|J_1 + J_2| > |J_3|$ and $|J_1| > |J_2|$ ($|J_1| < |J_2|$), Fig. 3(b) [Fig. 3(c)] shows that the corresponding oscillation center becomes 0.5 (–0.5). These oscillation centers are also insensitive to the presence of smaller long-range couplings, as shown in Figs. 3(a)–3(c). Using Eq. (10), the topological winding number values are measured as twice the oscillation centers.

Molecular topological edge states also can be detected by spin dynamics. As an example, we show how to detect the left topological edge state. To detect such an edge state, the system is initialized into the single spin-up excitation state $|\psi(t=0)\rangle = |\uparrow\downarrow\cdots\downarrow\downarrow\rangle$, with the single molecules trapped at the leftmost a -type tweezer flipped into the spin-up state. For the system in the topological phase $\nu = 1$, the initial state $|\psi(t=0)\rangle$ has a large overlap with the wave function of the left topological edge state, thus the left zero-energy edge mode is excited. Consequently, the time evolution of $|\psi(t=0)\rangle$ is basically decided by the left edge mode. This point is numerically confirmed in Fig. 3(d) by the dynamics of

$|\psi(t=0)\rangle$), which displays that the spin-up density is always maximal in the leftmost a -type (odd parity) lattice site and primarily distributed in the a -type sublattice, in accordance with the characteristic of the left topological edge state in the topological phase $\nu = 1$. Figure 3(d) also indicates that the wave packet partially propagates into the b -type sublattices. This is due to finite-size effect which causes a coupling between the left and right edge states. In contrast, for the trivial topological phase $\nu = 0$ and in the absence of the left topological edge state, the initial state $|\psi(t=0)\rangle$ in this case is a superposition of different bulk eigenmodes. As shown by its time evolution in Fig. 3(e), the wave packet evolves into the bulk, without edge localization behavior, showing the absence of the edge state. In a similar way, to detect the left edge state associated with the topological phases $\nu = -1$, the left edge mode is excited by initializing the system into $|\psi(t=0)\rangle = |\downarrow\uparrow\downarrow\cdots\downarrow\rangle$. From its time evolution shown in Fig. 3(f), we can see that the spin-up density is always maximal in the leftmost b -type (even parity) lattice site and mostly distributed in the b -type sublattice, conforming to the characteristics of the left edge state in the topological phase $\nu = -1$.

IV. INTERACTING SYMMETRY-PROTECTED TOPOLOGICAL PHASES

A. Interacting topological phases

We further study the many-particle topological properties in the optical tweezer ladder. As we will demonstrate, the system at half filling has a nonzero excitation gap. The resulting many-body gapped phase is an interacting SPT phase that is a developing class of exotic topological phases and currently is highly perused [62–68]. The SPT phase is characterized by nonlocal string-order parameters [69,70], lacking local order parameters. For our system, as demonstrated below, there exist two different nontrivial SPT phases, labeled type-I and type-II SPT phases, featuring different edge states. Specifically, the topological natures of gapped ground states in the type-I and type-II SPT phases are, respectively, characterized by the following two nonlocal string-order parameters:

$$\begin{aligned} O_I &= -\langle Z_{b_1} e^{i\frac{\pi}{2} \sum_{i=2}^{N-1} (Z_{a_i} + Z_{b_i})} Z_{a_N} \rangle, \\ O_{II} &= -\langle Z_{a_1} e^{i\frac{\pi}{2} \sum_{i=2}^{N-1} (Z_{a_i} + Z_{b_i})} Z_{b_N} \rangle, \end{aligned} \quad (11)$$

where $Z_c = 1 - 2c_i^\dagger c_i$ ($c = a, b$). To be specific, the nontrivial SPT phases are distinguished from the trivial ones by nonzero string-order parameters. Figure 4(a) presents the numerical results of O_I and O_{II} as a function of d_1/d_2 . As shown, the value of O_I (O_{II}) is finite for $d_1/d_2 < 0.54$ ($d_1/d_2 > 1.86$), the system is therefore in the type-I (type-II) SPT phase; While for $0.54 < d_1/d_2 < 1.86$, both O_I and O_{II} vanish and the system is in the trivial SPT phase.

Another signature associated with nontrivial SPT phases is the fourfold degeneracy of ground states. In Figs. 4(b)–4(d), based on exact diagonalization, we calculate the full energy spectrum of the system under OBCs as a function of the number of hard-core particles for a lattice size $N = 16$. As shown in Fig. 4(b), for the system in the trivial SPT phase,

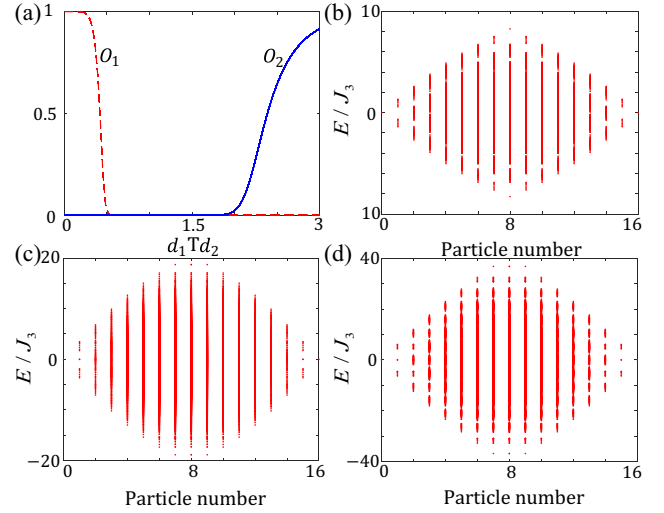


FIG. 4. (a) Nonlocal string-order parameters as a function of d_1/d_2 . Full energy spectra as a function of particle number for the many-particle system in the (b) trivial SPT phase and nontrivial (c) type-I and (d) type-II SPT phases. The systematic parameters are (b) $d_2 = 1.2d_1$, $J_1 = -0.25J_3$, and $J_2 = -0.14J_3$, (c) $d_2 = 2.5d_1$, $J_1 = -2.54J_3$, and $J_2 = -0.16J_3$, and (d) $d_2 = d_1/3$, $J_1 = -0.19J_3$, and $J_2 = -5.19J_3$. The lattice size is $N = 16$.

there is a single gapped ground state at half filling (the case of eight particles). In contrast, for the system in the nontrivial type-I and type-II SPT phases, as displayed in Figs. 4(c) and 4(d), respectively, the corresponding gapped ground states have fourfold degeneracy, including the ground states in the cases of seven, eight (twofold degenerate), and nine particles.

The ground-state degeneracy can be directly observed in the perfectly dimerized limits. For the case of a trivial SPT phase in the limit $J_1 = J_2 = 0$ and $J_3 < 0$, there is a single ground state that can be analytically derived as $|G\rangle = \prod_{i=1}^N (a_i^\dagger + b_i^\dagger) / \sqrt{2} |00\rangle_{a,b}$, while for the type-I SPT phase in the limit $J_2 = J_3 = 0$ and $J_1 < 0$, there are four ground states $|G_{x,y}^I\rangle = |xy\rangle_{a_1 b_N} \prod_{i=1}^N (b_i^\dagger + a_{i+1}^\dagger) / \sqrt{2} |00\rangle_{b_1 a_{i+1}}$, with $x, y \in \{0, 1\}$; Similarly, for the type-II SPT phase with $J_1 = J_3 = 0$ and $J_2 < 0$, the four ground states are $|G_{x,y}^{II}\rangle = |xy\rangle_{b_1 a_N} \prod_{i=1}^N (a_i^\dagger + b_{i+1}^\dagger) / \sqrt{2} |00\rangle_{a, b_{i+1}}$. As shown, the lattice ends a_1 and b_N (b_1 and a_N) in the SPT phases are decoupled from the Hamiltonian in the perfectly dimerized limits, which results in two zero-energy edge modes. As a consequence, the energies costed for zero, one, and two particles occupying the two zero-energy edge modes are the same. For example, for a 16-site lattice with eight particles filled (half-filling), in addition to seven particles occupying the bulk modes, one particle left for occupying the two zero-energy edge modes (two lattice ends), leading to twofold degenerate ground states; for seven or nine particles fillings, zero or two particles, respectively, occupy the two zero-energy edge modes, giving rise to two more degenerate ground states. Consequently, the four ground states in the type-I or type-II SPT phases are degenerate.

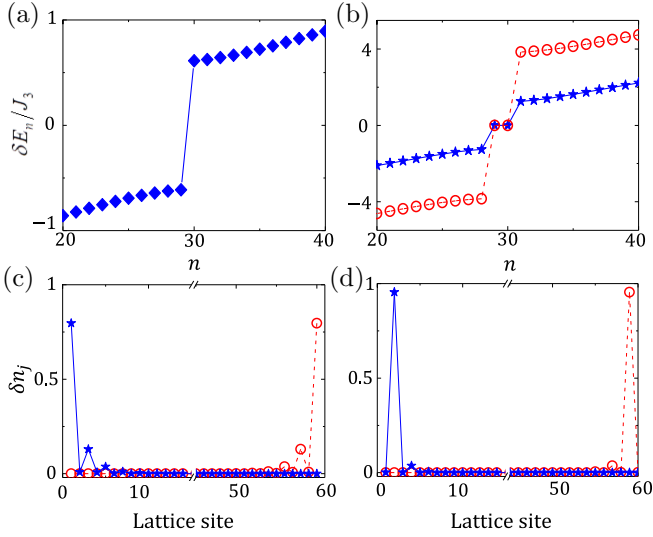


FIG. 5. The quasiparticle energy spectra as a function of particle number for the many-body system in the (a) trivial SPT phase and nontrivial (b) type-I (circles) and type-II (stars) SPT phases. The particle density distribution for the left (star) and right (circle) in-gap quasienergy edge modes in the type-I and type-II SPT phases are, respectively, shown in (c) and (d). The systematic parameters are (a) $d_2 = 1.2d_1$, $J_1 = -0.25J_3$, and $J_2 = -0.14J_3$, (b) $d_2 = 2.5d_1$, $J_1 = -2.54J_3$, and $J_2 = -0.16J_3$ (stars), and $d_2 = d_1/3$, $J_1 = -0.19J_3$, and $J_2 = -5.19J_3$ (circles). The lattice size is $N = 60$.

B. Edge states in quasiparticle energy spectrum

The appearance of in-gap edge states are a hallmark of nontrivial topological phases. Here we show that, for nontrivial interacting SPT phases, there are two in-gap edge modes in the quasiparticle energy spectrum. Suppose E_n^g is the ground-state energy of the system (under OBCs), with n particles populated inside. The quasiparticle energy spectrum is calculated as

$$\delta E_n = E_{n+1}^g - E_n^g, \quad (12)$$

where δE_n is the energy for adding one particle to a system with n particles. In Figs. 5(a) and 5(b), we use density matrix renormalization group method to calculate the quasiparticle energy spectra of the system, for a larger lattice size $N = 60$, taking into account long-range couplings. For the system in the trivial SPT phase, Figure 5(a) shows that there is no eigenmode in the quasiparticle energy gap around the half filling. By contrast, for the case of nontrivial type-I and type-II SPT phases shown in Fig. 5(b), there is one pair of in-gap modes at the zero quasiparticle energy.

To demonstrate that the in-gap zero-energy modes are corresponding to edge states, we further numerically calculate their density distributions. The particle density distribution for the quasiparticle eigenmodes is defined as

$$\delta n_j = \langle \psi_{n+1}^g | \hat{n}_j | \psi_{n+1}^g \rangle - \langle \psi_n^g | \hat{n}_j | \psi_n^g \rangle, \quad (13)$$

where $|\psi_n^g\rangle$ is the ground-state wave function of the system populating n particles. Figures 5(c) and 5(d) plot the density distributions of the two in-gap zero-energy modes, respectively, for the system in the type-I and type-II SPT phases. As shown, the particle density maximally distribute on the two edges, verifying that the two degenerate zero-energy in-gap

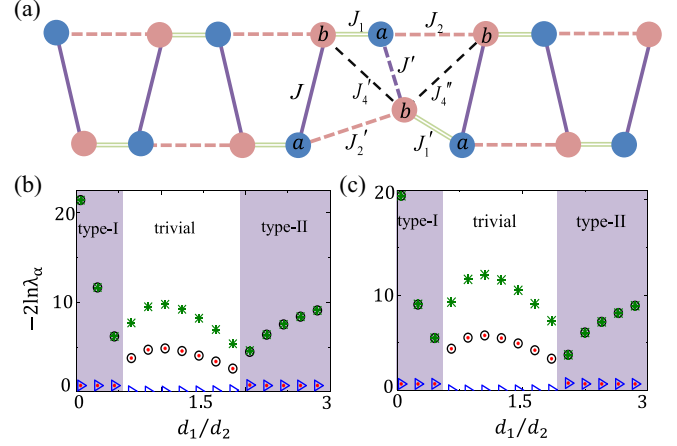


FIG. 6. (a) An optical tweezer ladder perturbed by one random tweezer out of the ladder. Low-lying entanglement spectra as a function of d_1/d_2 for the Hamiltonian (b) without and (c) with such perturbations. Triangles, points, circles, and stars, respectively, represent the lowest four levels.

modes are the left and right edge states. Interestingly, we find that the quasiparticle edge states in the interacting SPT phases have the same localization features as those in noninteracting topological phases. That is, the left (right) edge state in the type-I SPT phase only occupies the a -type (b -type) sublattices, whereas the left (right) edge state in the type-II SPT phase only populates the b -type (a -type) sublattices. Such a feature allows us to distinguish the type-I and type-II interacting SPT phases.

C. Symmetry-protected robustness

The SPT phases in the dipolar tweezer ladder are protected by the following symmetry: $UHU^{-1} = H$ [62–68], where the symmetry operator is defined as $U = \prod_i (a_i + a_i^\dagger)(b_i + b_i^\dagger)K$, with K being complex conjugation. We now show that the topological properties of SPT phases are robust to small perturbations that respect this symmetry. As shown in Fig. 6(a), small perturbations are introduced by shifting one of the middle b -type tweezers out of the ladder, which leads to couplings breaking chiral symmetry. Consequently, this small perturbation affects the topological properties associated with previously discussed single-particle topological phases. In contrast, it respects the symmetry operation U , thus it does not affect the characteristics of SPT phases. Through numerical calculations, we have checked that the influences on the string-order parameters, ground-state degeneracy, and quasiparticle edge states are minor, as compared to Figs. 4 and 5. To clearly see the symmetry-protected robustness, we exhibit the change of entanglement spectrum that is more sensitive to perturbations. For SPT phases, it is well-known that the entanglement spectrum features double degeneracy [71]. As shown in Figs. 6(b) and 6(c), in comparison with the case without perturbations, the entanglement spectrum distribution in the presence of small perturbations has a slight change, but in the nontrivial SPT phase regions the double degeneracy of the entire spectrum remains unchanged. This proves that the SPT phases are protected by

the symmetry U and robust to small symmetry-preserving perturbations.

D. Experimental detection

Before summarizing, we give a brief comment on the experimental detection of interacting SPT phases. Notably, in two very recent experiments, both the edge states and string-order parameters for characterizing SPT phases have been successfully probed in ultracold atom systems [55,72] by using site- and spin-resolved measurements and detecting nonlocal correlation functions. The strategy demonstrated there also can be applied to our proposed ultracold molecules system. For example, using coherent microwave spectroscopy technique, with their verified strategy one can directly measure magnetization distributions in the optical tweezer ladder to reveal the edge states and their localization features, and perform density-density correlation measurements to extract the two different nonlocal string-order parameters.

V. SUMMARY AND OUTLOOK

In summary, we have shown that an optical tweezer ladder of ultracold molecules can be naturally programmed to implement a generalized topological Su-Schrieffer-Heeger model. As demonstrated, such a ladder system possesses two different chiral topological phases at the single-particle level and features two different interacting SPT phases at the many-particle level. With the state of the art in ultracold molecules, all

signatures associated with these topological phases can be unambiguously probed. Our study exhibits that programmable optical tweezer arrays can open up more possibilities for implementing different topological spin lattice models and exploring diverse ultracold molecular topological phases.

In the near future, it would be quite interesting to study how to reconfigure high-dimensional optical tweezer arrays and tailor the long-range dipolar interactions for creating and exploring high-order topological phases [73–75] or even amorphous topological phases [76,77]. Moreover, taking into account interactions in this platform also provides possibilities for realizing and understanding high-dimensional interacting symmetry-SPT phases [64].

ACKNOWLEDGMENTS

This work was supported by the National Key Research and Development Program of China (Grant No. 2017YFA0304203), National Natural Science Foundation of China (NSFC) (Grants No. 12034012, No. 12074234, and No. 12074231), Changjiang Scholars and Innovative Research Team in University of Ministry of Education of China (PCSIRT)(IRT_17R70), Fund for Shanxi 1331 Project Key Subjects Construction, 111 Project (No. D18001), and Scientific and Technological Innovation Programs of Higher Education Institutions in Shanxi (No. 2020L0019). J.Z.J. and J.H.Z. contributed equally to this work.

-
- [1] D. DeMille, *Phys. Rev. Lett.* **88**, 067901 (2002).
 - [2] A. André, D. DeMille, J. M. Doyle, M. D. Lukin, S. E. Maxwell, P. Rabl, R. J. Schoelkopf, and P. Zoller, *Nat. Phys.* **2**, 636 (2006).
 - [3] S. F. Yelin, K. Kirby, and R. Côté, *Phys. Rev. A* **74**, 050301(R) (2006).
 - [4] E. Charron, P. Milman, A. Keller, and O. Atebek, *Phys. Rev. A* **75**, 033414 (2007).
 - [5] K. K. Ni, T. Rosenband, and D. D. Grimes, *Chem. Sci.* **9**, 6830 (2018).
 - [6] M. Hughes, M. D. Frye, R. Sawant, G. Bhole, J. A. Jones, S. L. Cornish, M. R. Tarbutt, J. M. Hutson, D. Jaksch, and J. Mur-Petit, *Phys. Rev. A* **101**, 062308 (2020).
 - [7] R. Sawant, J. A. Blackmore, P. D. Gregory, J. Mur-Petit, D. Jaksch, J. Aldegunde, J. M. Hutson, M. R. Tarbutt, and S. L. Cornish, *New J. Phys.* **22**, 013027 (2020).
 - [8] A. Micheli, G. K. Brennen, and P. Zoller, *Nat. Phys.* **2**, 341 (2006).
 - [9] R. Barnett, D. Petrov, M. D. Lukin, and E. Demler, *Phys. Rev. Lett.* **96**, 190401 (2006).
 - [10] H. P. Büchler, A. Micheli, and P. Zoller, *Nat. Phys.* **3**, 726 (2007).
 - [11] A. V. Gorshkov, S. R. Manmana, G. Chen, J. Ye, E. Demler, M. D. Lukin, and A. M. Rey, *Phys. Rev. Lett.* **107**, 115301 (2011).
 - [12] A. V. Gorshkov, S. R. Manmana, G. Chen, E. Demler, M. D. Lukin, and A. M. Rey, *Phys. Rev. A* **84**, 033619 (2011).
 - [13] M. A. Baranov, M. Dalmonte, G. Pupillo, and P. Zoller, *Chem. Rev.* **112**, 5012 (2012).
 - [14] K. R. A. Hazzard, S. R. Manmana, M. Foss-Feig, and A. M. Rey, *Phys. Rev. Lett.* **110**, 075301 (2013).
 - [15] B. Yan, S. A. Moses, B. Gadway, J. P. Covey, K. R. A. Hazzard, A. M. Rey, D. S. Jin, and J. Ye, *Nature (London)* **501**, 521 (2013).
 - [16] K. R. A. Hazzard, B. Gadway, M. Foss-Feig, B. Yan, S. A. Moses, J. P. Covey, N. Y. Yao, M. D. Lukin, J. Ye, D. S. Jin, and A. M. Rey, *Phys. Rev. Lett.* **113**, 195302 (2014).
 - [17] N. Y. Yao, M. P. Zaletel, D. M. Stamper-Kurn, and A. Vishwanath, *Nat. Phys.* **14**, 405 (2018).
 - [18] J. A. Blackmore, L. Caldwell, P. D. Gregory, E. M. Bridge, R. Sawant, J. Aldegunde, J. Mur-Petit, D. Jaksch, J. M. Hutson, B. E. Sauer, M. R. Tarbutt, and S. L. Cornish, *Quantum Sci. Technol.* **4**, 014010 (2019).
 - [19] R. V. Krems, *Phys. Chem. Chem. Phys.* **10**, 4079 (2008).
 - [20] N. Balakrishnan, *J. Chem. Phys.* **145**, 150901 (2016).
 - [21] M. S. Safronova, D. Budker, D. DeMille, Derek F. Jackson Kimball, A. Derevianko, and C. W. Clark, *Rev. Mod. Phys.* **90**, 025008 (2018).
 - [22] C. Chin, V. V. Flambaum, and M. G. Kozlov, *New J. Phys.* **11**, 055048 (2009).
 - [23] A. M. Kaufman and K. K. Ni, *Nat. Phys.* **17**, 1324 (2021).
 - [24] L. R. Liu, J. D. Hood, Y. Yu, J. T. Zhang, N. R. Hutzler, T. Rosenband, and K. K. Ni, *Science* **360**, 900 (2018).

- [25] L. Anderegg, L. W. Cheuk, Y. Bao, S. Burchesky, W. Ketterle, K. K. Ni, and J. M. Doyle, *Science* **365**, 1156 (2019).
- [26] L. R. Liu, J. D. Hood, Y. Yu, J. T. Zhang, K. Wang, Y. W. Lin, T. Rosenband, and K. K. Ni, *Phys. Rev. X* **9**, 021039 (2019).
- [27] J. T. Zhang, Y. Yu, W. B. Cairncross, K. Wang, L. R. B. Picard, J. D. Hood, Y. W. Lin, J. M. Hutson, and K. K. Ni, *Phys. Rev. Lett.* **124**, 253401 (2020).
- [28] J. D. Hood, Y. Yu, Y. W. Lin, J. T. Zhang, K. Wang, L. R. Liu, B. Gao, and K. K. Ni, *Phys. Rev. Research* **2**, 023108 (2020).
- [29] L. W. Cheuk, L. Anderegg, Y. Bao, S. Burchesky, S. S. Yu, W. Ketterle, K. K. Ni, and J. M. Doyle, *Phys. Rev. Lett.* **125**, 043401 (2020).
- [30] X. He, K. Wang, J. Zhuang, P. Xu, X. Gao, R. Guo, C. Sheng, M. Liu, J. Wang, J. Li, G. V. Shlyapnikov, and M. Zhan, *Science* **370**, 331 (2020).
- [31] W. B. Cairncross, J. T. Zhang, L. R. B. Picard, Y. Yu, K. Wang, and K. K. Ni, *Phys. Rev. Lett.* **126**, 123402 (2021).
- [32] S. Burchesky, L. Anderegg, Y. Bao, S. S. Yu, E. Chae, W. Ketterle, K. K. Ni, and J. M. Doyle, *Phys. Rev. Lett.* **127**, 123202 (2021).
- [33] Y. Yu, K. Wang, J. D. Hood, L. R. B. Picard, J. T. Zhang, W. B. Cairncross, J. M. Hutson, R. Gonzalez-Ferez, T. Rosenband, and K. K. Ni, *Phys. Rev. X* **11**, 031061 (2021).
- [34] L. Anderegg, S. Burchesky, Y. Bao, S. S. Yu, T. Karman, E. Chae, K. K. Ni, W. Ketterle, and J. M. Doyle, *Science* **373**, 779 (2021).
- [35] M. Sroczynska, A. Dawid, M. Tomza, Z. Idziaszek, T. Calarco, and K. Jachymski, *New J. Phys.* **24**, 015001 (2022).
- [36] J. T. Zhang, L. R. B. Picard, W. B. Cairncross, K. Wang, Y. Yu, F. Fang, and K. K. Ni, [arXiv:2112.00991v1](https://arxiv.org/abs/2112.00991v1).
- [37] L. D. Carr, D. DeMille, R. V. Krems, and J. Ye, *New J. Phys.* **11**, 055049 (2009).
- [38] J. L. Bohn, M. Rey, and J. Ye, *Science* **357**, 1002 (2017).
- [39] S. A. Moses, J. P. Covey, M. T. Miecnikowski, D. S. Jin, and J. Ye, *Nat. Phys.* **13**, 13 (2017).
- [40] M. Z. Hasan and C. L. Kane, *Rev. Mod. Phys.* **82**, 3045 (2010).
- [41] X. L. Qi and S. C. Zhang, *Rev. Mod. Phys.* **83**, 1057 (2011).
- [42] N. Goldman, J. C. Budich, and P. Zoller, *Nat. Phys.* **12**, 639 (2016).
- [43] D. W. Zhang, Y. Q. Zhu, Y. X. Zhao, H. Yan, and S. L. Zhu, *Adv. Phys.* **67**, 253 (2018).
- [44] N. R. Cooper, J. Dalibard, and I. B. Spielman, *Rev. Mod. Phys.* **91**, 015005 (2019).
- [45] L. Lu, J. D. Joannopoulos, and M. Soljac, *Nat. Photonics* **8**, 821 (2014).
- [46] X. Zhang, M. Xiao, Y. Cheng, M. H. Lu, and J. Christensen, *Commun. Phys.* **1**, 97 (2018).
- [47] T. Ozawa, H. M. Price, A. Amo, N. Goldman, M. Hafezi, L. Lu, M. C. Rechtsman, D. Schuster, J. Simon, O. Zilberberg, and I. Carusotto, *Rev. Mod. Phys.* **91**, 015006 (2019).
- [48] G. Ma, M. Xiao, and C. T. Chan, *Nat. Rev. Phys.* **1**, 281 (2019).
- [49] N. Y. Yao, C. R. Laumann, A. V. Gorshkov, S. D. Bennett, E. Demler, P. Zoller, and M. D. Lukin, *Phys. Rev. Lett.* **109**, 266804 (2012).
- [50] D. Peter, N. Y. Yao, N. Lang, S. D. Huber, M. D. Lukin, and H. P. Büchler, *Phys. Rev. A* **91**, 053617 (2015).
- [51] N. Y. Yao, A. V. Gorshkov, C. R. Laumann, A. M. Lauchli, J. Ye, and M. D. Lukin, *Phys. Rev. Lett.* **110**, 185302 (2013).
- [52] S. V. Syzranov, M. L. Wall, B. Zhu, V. Gurarie, and A. M. Rey, *Nat. Commun.* **7**, 13543 (2016).
- [53] T. Schuster, F. Flicker, M. Li, S. Kotochigova, J. E. Moore, J. Ye, and N. Y. Yao, *Phys. Rev. A* **103**, 063322 (2021).
- [54] T. Schuster, F. Flicker, M. Li, S. Kotochigova, J. E. Moore, J. Ye, and N. Y. Yao, *Phys. Rev. Lett.* **127**, 015301 (2021).
- [55] S. de Léséleuc, V. Lienhard, P. Scholl, D. Barredo, S. Weber, N. Lang, H. P. Büchler, T. Lahaye, and A. Browaeys, *Science* **365**, 775 (2019).
- [56] W. P. Su, J. R. Schrieffer, and A. J. Heeger, *Phys. Rev. Lett.* **42**, 1698 (1979).
- [57] F. Mei, G. Chen, L. Tian, S. L. Zhu, and S. Jia, *Phys. Rev. A* **98**, 012331 (2018).
- [58] F. Cardano, A. D. Errico, A. Dauphin, M. Maffei, B. Piccirillo, C. de Liso, G. D. Filippis, V. Cataudella, E. Santamato, L. Marrucci, M. Lewenstein, and P. Massignan, *Nat. Commun.* **8**, 15516 (2017).
- [59] E. J. Meier, F. A. An, A. Dauphin, M. Maffei, P. Massignan, T. L. Hughes, and B. Gadway, *Science* **362**, 929 (2018).
- [60] D. Xie, W. Gou, T. Xiao, B. Gadway, and B. Yan, *npj Quantum Inf.* **5**, 55 (2019).
- [61] K. Shiozaki and S. Fujimoto, *Phys. Rev. Lett.* **110**, 076804 (2013).
- [62] X. Chen, Z. C. Gu, and X. G. Wen, *Phys. Rev. B* **83**, 035107 (2011).
- [63] F. Pollmann, E. Berg, A. M. Turner, and M. Oshikawa, *Phys. Rev. B* **85**, 075125 (2012).
- [64] X. Chen, Z. X. Liu, and X. G. Wen, *Phys. Rev. B* **84**, 235141 (2011).
- [65] N. Schuch, D. Pérez-García, and I. Cirac, *Phys. Rev. B* **84**, 165139 (2011).
- [66] X. Chen, Z. C. Gu, Z. X. Liu, and X. G. Wen, *Science* **338**, 1604 (2012).
- [67] F. Pollmann and A. M. Turner, *Phys. Rev. B* **86**, 125441 (2012).
- [68] R. Verresen, R. Moessner, and F. Pollmann, *Phys. Rev. B* **96**, 165124 (2017).
- [69] M. den Nijs and K. Rommelse, *Phys. Rev. B* **40**, 4709 (1989).
- [70] T. Kennedy and H. Tasaki, *Phys. Rev. B* **45**, 304 (1992).
- [71] F. Pollmann, A. M. Turner, E. Berg, and M. Oshikawa, *Phys. Rev. B* **81**, 064439 (2010).
- [72] P. Sompet, S. Hirthe, D. Bourgund, T. Chalopin, J. Bibo, J. Koepsell, P. Bojović, R. Verresen, F. Pollmann, G. Salomon, C. Gross, T. A. Hilker, and I. Bloch, *Nature* **606**, 484 (2022).
- [73] W. A. Benalcazar, B. A. Bernevig, and T. L. Hughes, *Science* **357**, 61 (2017).
- [74] F. Schindler, A. M. Cook, M. G. Vergniory, Z. Wang, S. S. P. Parkin, B. A. Bernevig, and T. Neupert, *Sci. Adv.* **4**, eaat0346 (2018).
- [75] B. Xie, H. X. Wang, X. Zhang, P. Zhan, J. H. Jiang, M. Lu, and Y. Chen, *Nat. Rev. Phys.* **3**, 520 (2021).
- [76] A. Agarwala and V. B. Shenoy, *Phys. Rev. Lett.* **118**, 236402 (2017).
- [77] N. P. Mitchell, L. M. Nash, D. Hexner, A. M. Turner, and W. T. M. Irvine, *Nat. Phys.* **14**, 380 (2018).